crystals

MDPI

Article

Experimental and Simulation Study on the Transformation Behavior of Q580R Steel Under Continuous Cooling Conditions

Weina Han, Jianping Wang *, Jianing Lei, Jinyu Ni and Jinliang Bai

Liaoning Provincial Key Laboratory of Energy Storage and Utilization, Yingkou Institute of Technology, Yingkou 115014, China; hanweina@yku.edu.cn (W.H.); 15504070109@163.com (J.L.); 19553078567@163.com (J.N.); 15504079808@163.com (J.B.)

* Correspondence: wangjianping@yku.edu.cn

Abstract

To reveal the controlling mechanism of cooling rate on the continuous cooling transformation, microstructure evolution and mechanical performances of Q580R low-temperature pressure vessel steel, this study took industrial-scale Q580R steel as the research object. The JMatPro thermodynamic software was utilized for simulating and calculating its equilibrium phase diagram, TTT diagram, CCT diagram and mechanical property evolution. Continuous cooling experiments with a wide range of cooling rates between 0.1 and 50 °C/s were executed on a Gleeble-3500 thermal simulator. Combined with optical microscopy, scanning electron microscopy and Vickers hardness tester for microstructure characterization and property testing, the measured CCT diagram was constructed and contrasted with the simulation results for verification. Experimentally, the phase composition of Q580R steel evolves at regular intervals with cooling rate. As the cooling rate rises, the ferrite content constantly decreases, the bainite content first increases and subsequently decreases, and the martensite content constantly increases. When the cooling rate reaches 30 °C/s, the martensite proportion can exceed 90%, and the microstructure is significantly refined. The hardness of the material first increases rapidly and subsequently trends to be steady as the cooling rate rises, reaching 308 HV_{10} at 50 °C/s. The measured transformation law, microstructure evolution and hardness change exceedingly corresponds to the JMatPro simulation results. This validates the credibility of the simulation prediction. This study clarifies the quantitative relationship among "cooling rate-microstructure-properties" of Q580R steel, which can provide theoretical basis and data support for the precise design of heat treatment process and the optimization of strength and toughness. The established relationship can directly guide the formulation of controlled cooling parameters during hot rolling and off-line quenching and tempering production of Q580R pressure vessel plates, helping manufacturers optimize industrial heat-treatment procedures to satisfy low-temperature toughness requirements for petrochemical and cryogenic pressure vessel service.

Keywords: Q580R steel; JMatPro; phase transformation; cooling rate; microstructure

Check for updates

Academic Editor: Mattia Franceschi

Received: 6 May 2026
Revised: 17 June 2026
Accepted: 18 June 2026
Published: 21 June 2026

Copyright: © 2026 by the authors. Licensee MDPI, Basel, Switzerland. This article is an open access article distributed under the terms and conditions of the Creative Commons Attribution (CC BY) license.

1. Introduction

Q580R steel is characterized by low-carbon microalloying and quenching-tempering modification. It combines high strength, good plasticity, excellent low-temperature toughness at −20 °C, stable weldability and fatigue resistance, making it a key structural material for lightweight, high-pressure and long-life service of pressure equipment. It is widely used

in petrochemical pressure vessels, energy equipment, heavy machinery, marine engineering, special equipment and other industrial fields with strict requirements for strength and safety [1–8]. Under complex service conditions like corrosive media, elevated temperature, high pressure and alternating loads, Q580R steel undertakes multiple tasks of structural bearing, medium sealing and long-term safe and stable operation. Its microstructure uniformity, phase composition stability and strength-toughness matching directly determine the service life and operational reliability of equipment. With the rapid development of pressure equipment towards large-scale, high-parameter and thick-specification, the engineering site has put forward more stringent requirements for the Q580R steel's strength stability, microstructure uniformity and heat treatment adaptability.

Continuous cooling transformation (CCT) works as the core link determining the high-strength steel's mechanical performances and microstructure. Cooling rate can significantly regulate phase composition, grain size and comprehensive material properties, which is the key theoretical basis for the precise design of heat treatment processes. Harvanec et al. [9] established the in situ continuous cooling transformation diagram of S960 high-strength steel under welding thermal cycle, clarifying the dominant role of thermal history in the transformation law during welding. Wang et al. [10] systematically studied the impact of initial transformation temperature upon the microstructural features and strength-toughness of bainitic steel, confirming that appropriately increasing the initial transformation temperature can effectively refine bainitic laths and achieve synergistic improvement of strength and toughness. Du et al. [11] conducted continuous cooling transformation research on medium manganese steel, and the results showed that increasing the cooling rate inhibits ferrite transformation while facilitating the formation of bainite and martensite. Castro et al. [12] investigated the influence of hot deformation on the transformation kinetics of carbide-free bainitic steel, finding that hot deformation accelerates bainite transformation and refines bainite morphology. Zhu et al. [13] studied the influence of Nb-W composite microalloying upon the CCT of low-alloy steel, confirming that this system can effectively expand the bainite transformation interval and improve the hardenability of steel. Yan et al. [14] revealed the dynamic CCT law of 55SiCr spring steel, clarifying that dynamic deformation reduces the key cooling rate of transformation and facilitates the acquisition of a refined microstructure. Li et al. [15] determined the CCT diagram of Si-Cu alloyed ductile iron, finding that its transformation only includes pearlite and martensite regions without a bainite transformation interval. Jiang et al. [16] compared the CCT of HSLA wear-resistant steels showing different compositions, concluding that increasing carbon and chromium contents broadens the bainite transformation interval and improves low-temperature impact toughness. Zhang et al. [17] analyzed the solid-state continuous cooling transformation characteristics of 45 steel under laser thermal action, clarifying the special microstructure evolution mechanism under rapid heating and quenching. Wang et al. [18] examined the influence of Nb microalloying upon the CCT of seismic reinforcement, confirming that Nb enhances austenite stability and promotes the formation of fine-grained microstructure. Pei et al. [19] studied the CCT characteristics of low-carbon high-strength steel and established a quantitative prediction model linking cooling rate and phase transformation parameters. Their model exhibited favorable agreement with experimental data and can guide controlled cooling optimization.

As a mature material thermodynamics and kinetics simulation software, JMatPro can accurately calculate equilibrium phase diagrams, TTT, CCT diagrams and mechanical properties. It has been applied in the transformation prediction and process optimization of steel, which can significantly reduce the number of tests and shorten the R&D cycle. Han et al. [20] studied the CCT of 9Ni steel by combining experiments and JMatPro simulation, and the simulation results agree well with the measured results, confirming

the credibility of software prediction. Pineda et al. [21] used JMatPro to analyze the austenite formation and decomposition law of high-strength steel during heating-cooling cycles, providing temperature parameters for thermal processing design. Dong et al. [22] calculated the solidification path of refractory multi-principal alloys based on JMatPro, realizing the regulation of eutectic microstructure and optimization of high-temperature properties. Krbata et al. [23] simulated the continuous cooling transformation of tool steel by JMatPro, establishing a quantitative correlation among cooling rate, microstructure, and hardness. Amiri et al. [24] combined JMatPro simulation and experimental characterization to reveal the microstructure evolution law of additively manufactured functionally graded materials. Sun et al. [25] used JMatPro to calculate the impact of alloying elements upon the high-temperature performances of titanium alloys, providing data support for alloy composition design. Chen et al. [26] optimized the heat treatment parameters of high-speed steel based on JMatPro simulation, achieving precise matching of microstructure and mechanical properties. Yu et al. [27] simulated the microstructure and performances of an iron-based surfacing layer by JMatPro, providing theoretical guidance for surfacing process optimization.

In summary, existing studies have confirmed that cooling rate is the core factor regulating high-strength steel's performance and microstructure, and JMatPro can effectively predict material transformation behavior. However, there is a lack of systematic research on the CCT law, the construction of a measured CCT diagram and verification of JMatPro simulation accuracy of Q580R low-temperature pressure vessel steel in a wide cooling rate range (0.1–50 °C/s). Based on this, this study takes industrial-scale Q580R steel as the object, adopts the method of JMatPro simulation + static thermal simulation + microstructure characterization + hardness test to reveal the regulation mechanism of cooling rate upon transformation behavior, microstructure and mechanical performances, construct the measured CCT diagram and verify the simulation reliability, providing a theoretical and practical support for the outstanding design of heat treatment, strength-toughness optimization and engineering application of Q580R steel. The optimized cooling parameters summarized in this work can be directly referenced by steel mills to reduce trial-production costs and improve the stability of the mechanical properties of finished Q580R plates for pressure equipment.

2. Experimental Materials and Research Methods

The experimental material is a 10 mm thick hot-rolled Q580R steel plate. It is rolled from a 150 mm thick cast slab after controlled rolling and controlled cooling. The tested steel's chemical composition at multiple points was measured by a SPECTROLAB M7 direct reading spectrometer (SPECTRO Analytical Instruments GmbH & Co. KG, Kleve, Germany) and the mean value was taken. The main chemical composition is displayed in Table 1, and all components meet the requirements of GB/T 713.6-2023 Steel Plates, Sheets and Strip for Pressure Equipments—Part 6: Quenched and Tempered High Strength Steels [28].

Table 1. Main chemical composition of Q580R steel (wt%).

C	Ni	Si	Mn	V	Ti	Al	Cr	Cu	Mo	Nb
0.074	0.391	0.235	1.21	0.04	0.014	0.023	0.284	0.192	0.156	0.022

In this study, JMatPro 7.0 (Sente Software Ltd., Guildford, Surrey, UK) software was utilized for numerical simulation. General steel was used as the material type, and the chemical composition of Q580R was input using the built-in database without modification. The Thermodynamic Properties module with "Step Temperature" function was employed

to figure out the thermodynamic phase diagram of Q580R steel from 25 °C to 1600 °C, clarifying the equilibrium phase composition and transformation temperature. In the Phase Transformations module, the "Advanced CCT" function was used to calculate the continuous cooling transformation (CCT) diagram. The austenitization conditions were consistent with the thermal simulation experiments: austenitization temperature of 920 °C; holding time of 3 min. The austenite decomposition behavior, room-temperature microstructure and mechanical property evolution under different cooling rates were analyzed.

Static thermal simulation tests were executed on a Gleeble-3500 thermal simulator (Dynamic Systems Inc., Poestenkill, NY, USA). To minimize the temperature gradient and ensure uniform and controllable cooling, cylindrical specimens with a diameter of 3 mm and a length of 10 mm were adopted. The specimen was clamped by copper electrodes at both ends to ensure a stable thermal field distribution and uniform heat transfer during heating and cooling. According to the Heat Treatment Handbook (4th ed., Vol. 2: Structural Steel Heat Treatment) [29], the specimen was heated to 920 °C at a heating rate of 10 °C/s and held for 3 min to ensure complete austenitization and stable grain size. Then, continuous cooling to room temperature was performed at 8 rates: 0.1, 0.5, 1, 5, 10, 20, 30, 50 °C/s. In the test, the closed-loop real-time temperature control system of the Gleeble-3500 simulator dynamically adjusted the cooling intensity based on the temperature signal fed back by the thermocouple, ensuring a strictly linear and constant cooling rate. The dilation-temperature-time curves were collected synchronously, and the tangent method was utilized for measuring the transformation start and end temperatures under each cooling rate.

After the thermal simulation experiment, the cylindrical specimen was cut along the diameter by wire cutting to prepare a rectangular section of 3 mm × 10 mm. Then, the specimen was fixed and encapsulated by cold mounting with epoxy resin to ensure complete edges during subsequent sample preparation. After mounting, the specimen was gradually polished with metallographic sandpaper and mechanically polished with W1.0 diamond polishing paste. The polished specimen was etched with a 4 vol% nitric acid alcohol solution, washed with anhydrous ethanol and fast dried with a blower to prepare a metallographic specimen. The Axioscope 5 optical microscope (OM) (Carl Zeiss Microscopy GmbH, Göttingen, Niedersachsen, Germany) and scanning electron microscope (SEM) (Carl Zeiss Microscopy GmbH, Göttingen, Niedersachsen, Germany) were used to observe the cross-sectional microstructure. The HV-1000 Vickers hardness tester (Shanghai Yanrun Optical-Mechanical Technology Co., Ltd., Shanghai, China) was used to test the cross-sectional hardness with a load of 10 kg and a loading time of 10 s. Five different areas were measured for each specimen, with the mean value being the final hardness.

3. Simulation Results and Analysis

3.1. Thermodynamic Phase Diagram Simulation

Figure 1 exhibits the full thermodynamic equilibrium phase diagram of Q580R steel computed by JMatPro. An additional phase diagram (Figure 2) is provided to specifically illustrate the temperature-dependent phase fraction evolution of the main low-content secondary precipitates with a mass fraction below 1 wt.%, eliminating the interference of high-content matrix phases to clearly visualize the precipitation behavior of trace strengthening phases. As shown in Figure 1, the phase diagram includes three primary matrix phases: liquid phase, austenite and ferrite, as well as 16 types of second phases such as sulfide (MnS), nitride (TiN, NbN), copper-rich phase (Cu), G phase, boride (M_3B_2), carbide (M_7C_3, M(C,N), $M_{23}C_6$), cementite, phosphide (M_2P, M_3P), which form a total of 19 phase regions. This is because Q580R contains not only Mn, Cr, Ni, Mo and other main alloying elements, but also Nb, V, Ti, B and other trace elements. These elements provide thermo-

dynamic and kinetic conditions for the precipitation of different types of second phases via element diffusion, interface adsorption and lattice distortion effects during cooling [30]. At 1600 °C, the alloy mainly exists in the liquid phase; ferrite precipitates preferentially at 1519 °C, and the alloy enters the liquid–solid two-phase area; when the temperature falls to 1485 °C, the liquid phase disappears completely, austenite begins to precipitate and its content increases rapidly, while ferrite content decreases gradually; at 1459 °C, ferrite dissolves completely, and austenite becomes the only matrix phase. Thereafter, austenite remains stable in the range of 1459–1118 °C with only trace element segregation and no obvious second phase precipitation. As shown in Figure 2, MnS, as the primary sulfide inclusion phase, initiates precipitation at 1400 °C during the solidification process, with a stable mass fraction of 0.02 wt.% in the full temperature range, which mainly affects the inclusion morphology and low-temperature toughness of the pressure vessel steel. Below 1118 °C, carbide M(C,N) starts precipitating, and the alloy enters the carbide precipitation interval. As a highly stable carbonitride, this phase not only inhibits austenite grain growth through the "grain boundary pinning" effect, but also remains dispersed during subsequent cooling, providing long-term high-temperature strength support for the alloy [31]. With the temperature further dropping to 837 °C, ferrite precipitates secondarily, and its content increases gradually with decreasing temperature, while austenite content decreases accordingly. Cementite exists stably in the range of 692–592 °C, reaching the maximum content of 0.78% at 662 °C. The precipitation of this phase can improve the hardness and strength of the alloy through dispersion strengthening, but excessive cementite tends to form a continuous distribution at grain boundaries, leading to a decrease in alloy toughness. At the same time, $M_{23}C_6$ begins to precipitate at 660 °C and its mass fraction increases continuously with decreasing temperature, reaching a peak of 0.93 wt.% at 90 °C. This phase disperses in the ferrite matrix and acts as the dominant low-temperature strengthening phase, synergistically improving the alloy strength with cementite. The overlapping precipitation interval of cementite and $M_{23}C_6$ in 600–660 °C leads to the competitive precipitation of the two phases, which is the main reason for the complex content variation trend of the two phases in this temperature range. In addition, M_7C_3 carbide precipitates in the medium temperature range of 500–700 °C, with a peak content of 0.48 wt.% at 600 °C, which further supplements the precipitation strengthening effect of the alloy. Below 300 °C, the copper-rich phase (Cu) initiates precipitation at 200 °C, with a stable mass fraction of 0.20 wt.% at room temperature, which provides additional age-strengthening effect for the alloy. It should be noted that such low-temperature equilibrium precipitates are predicted under ideal equilibrium conditions; their actual precipitation requires extremely long holding durations and hardly forms under conventional continuous cooling conditions applied in this work. The room-temperature equilibrium phase composition of Q580R steel takes ferrite as the main matrix phase, showing a content up to 97.85%, providing a good foundation for plasticity and toughness. The main strengthening phase system is composed of $M_{23}C_6$ (0.60 wt.%) and cementite (0.42 wt.%), which are the dominant secondary precipitates in the room-temperature microstructure. Through the synergistic effect of "dispersion strengthening + precipitation strengthening", the alloy achieves high strength [32]. In addition, the existence of trace second phases such as the copper-rich phase, M(C,N) and MnS provides key support for the balance of comprehensive properties of the alloy through age strengthening, grain refinement, machining performance regulation and other effects.

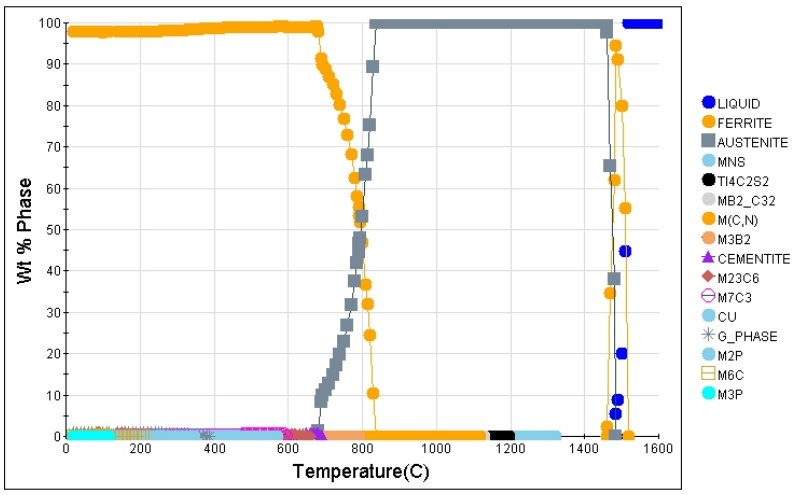


Figure 1. Full thermodynamic equilibrium phase diagram of Q580R steel.

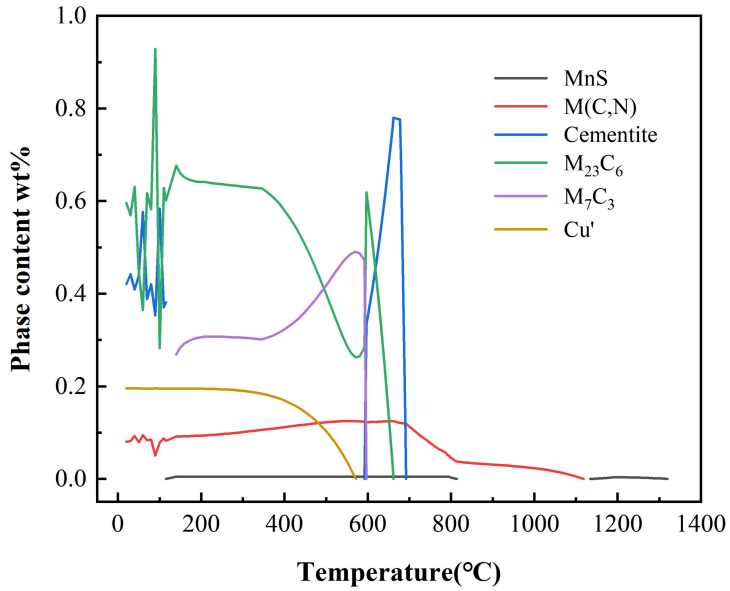


Figure 2. Thermodynamic equilibrium phase diagram of low-content precipitated phases of Q580R steel.

3.2. TTT Diagram Simulation

Figure 3 shows the TTT diagram of Q580R steel computed by JMatPro software. Obviously, the isothermal transformation of supercooled austenite of Q580R steel presents typical features of low-carbon alloy steel, including four transformation types: ferrite, pearlite, bainite and martensite. The maximum precipitation temperatures of ferrite, pearlite and bainite reach 837 °C, 697 °C and 611 °C, respectively. The "nose" temperature of ferrite reaches 640 °C with an incubation period of 3.7 s; the "nose" temperature of pearlite reaches 610 °C with an incubation period of 308.3 s; the "nose" temperature of bainite reaches 520 °C with an incubation period of 2.8 s. The shortest incubation period of bainite indicates that the steel has the strongest bainite transformation tendency and is suitable for obtaining bainite microstructure through isothermal holding. The martensite start transformation temperature is 441 °C, and the 90% transformation temperature reaches 333 °C. The TTT diagram shows that Q580R steel is dominated by ferrite-pearlite transformation in the high-temperature region of 570–837 °C, bainite transformation in the medium-low temperature region of 440–570 °C, and martensitic transformation below 440 °C. The transformation

law conforms to the characteristics of low-carbon modified pressure vessel steel, providing direct reference for heat treatment process formulation.

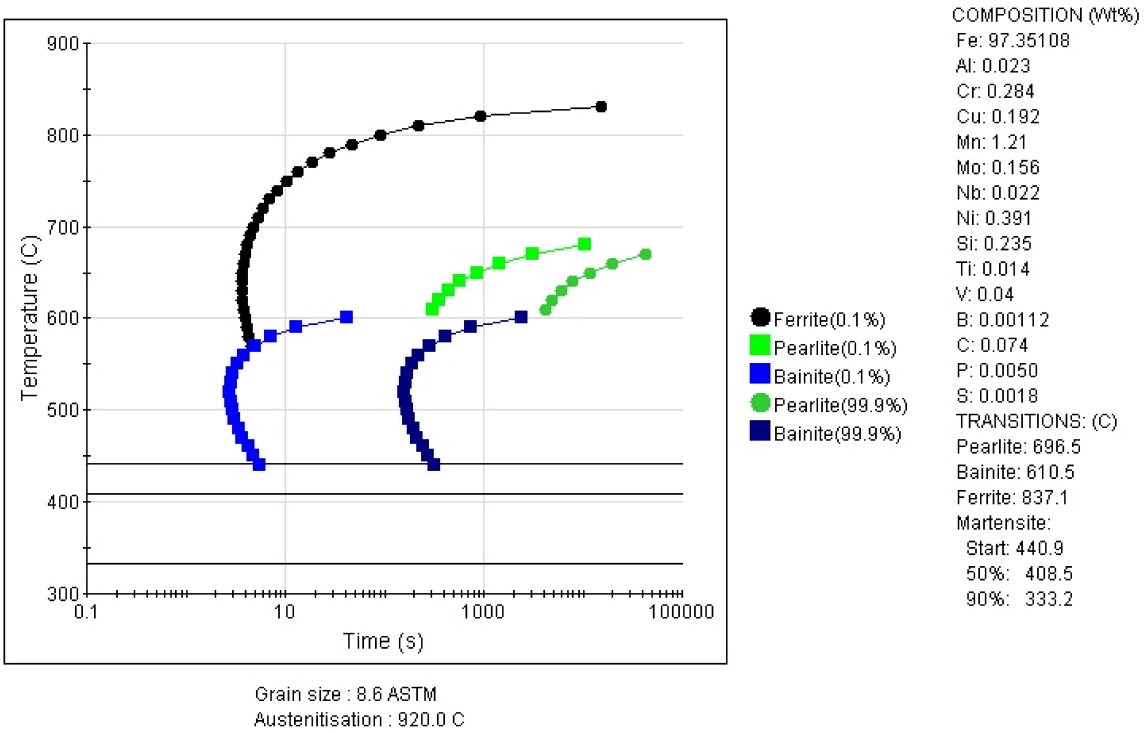


Figure 3. TTT diagram of Q580R steel.

3.3. CCT Diagram Simulation

Figure 4 shows the CCT diagram of Q580R steel computed by JMatPro. The room-temperature phase composition content corresponding to different cooling rates is shown in Table 2. As indicated in Figure 4 and Table 2, the A_3 temperature of Q580R steel is 837 °C, the A_1 temperature is 697 °C, M_s is 441 °C, and M_f is 311 °C. The start transformation temperature ranges of ferrite, pearlite and bainite reach 551–819 °C, 392–650 °C and 479–522 °C, respectively. When the cooling rate $\leq$ 0.5 °C/s, the room-temperature microstructure is mainly controlled by ferrite and a small amount of pearlite, with ferrite accounting for more than 98%; as the cooling rate reaches 1 °C/s, bainite begins to precipitate; when the cooling rate rises to 5 °C/s, pearlite disappears, bainite content increases rapidly to about 42%, ferrite content decreases to about 46%, and martensite begins to precipitate; when the cooling rate reaches 10 °C/s, the microstructure is mainly dominated by martensite, accounting for more than 70%, and bainite decreases to about 10%; when the cooling rate $\geq$ 20 °C/s, martensite accounts for more than 90%, bainite and ferrite contents are extremely low, and retained austenite remains at a negligible level. It can be seen that with the increase in cooling rate, ferrite content decreases continuously, bainite content first increases and then decreases, and martensite content increases continuously. The continuous transformation from ferrite-pearlite microstructure to bainite and martensite microstructure can be realized by regulating the cooling rate.

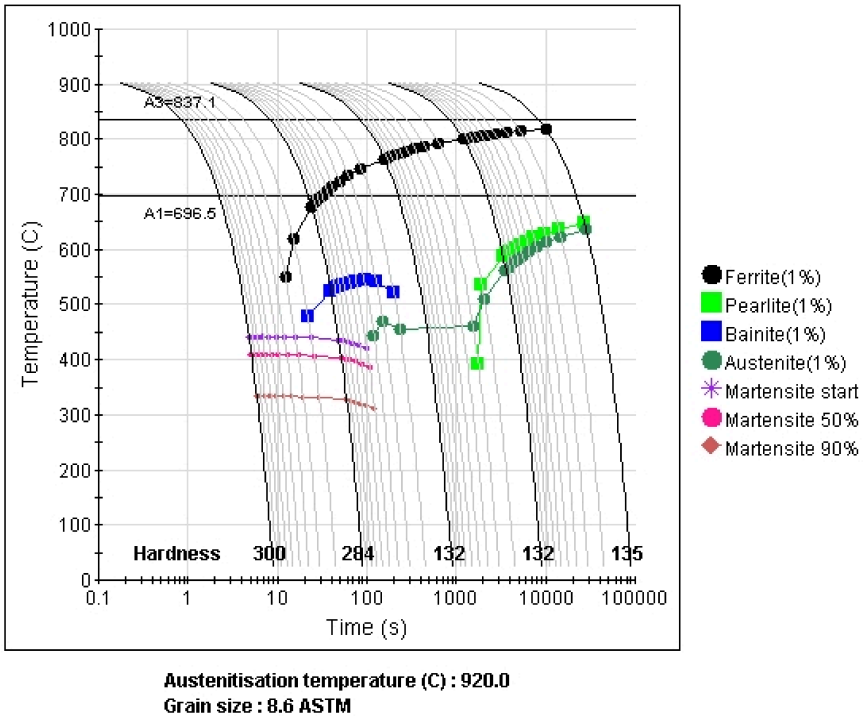


Figure 4. CCT diagram of Q580R steel.

Table 2. Room-temperature phase composition of Q580R steel at different cooling rates.

Cooling Rate/(°C/s)	0.1	0.5	1	5	10	20	30	50
Ferrite/%	98.1	98.4	97.5	46.1	18.8	4.5	1.7	0.5
Pearlite/%	1.9	0.3	0.1	—	—	—	—	—
Bainite/%	—	—	2.4	42.2	9.8	1.8	0.7	0.2
Martensite/%	—	—	—	11.7	71.4	93.7	97.6	99.3
Retained austenite/%	—	1.3	—	—	—	—	—	—

Note: The em dash (—) indicates that the corresponding phase cannot form under this cooling rate, and its volume fraction is 0%.

3.4. Mechanical Property Simulation

Figure 5 exhibits the mechanical property simulation results of Q580R steel. Yield strength, tensile strength, and hardness follow the identical trend: they increase rapidly at low cooling rates and then plateau. From 0.5 to 10 °C/s, the yield strength, tensile strength and hardness rise significantly. The reason is that the increase in cooling rate inhibits the nucleation and progress of ferrite in the high-temperature region, and the microstructure gradually changes from ferrite-dominated to hard phase-dominated, such as bainite and martensite. The synergy of grain refinement strengthening, dislocation strengthening and transformation strengthening is continuously enhanced, thus greatly improving the overall microstructure strengthening effect. When the cooling rate reaches more than 20 °C/s, the microstructure is mainly controlled by martensite. The strengthening effect caused by supersaturated solid solution and dislocation entanglement of martensite [33] makes the material's performance reach the peak and tends to be steady. When the cooling rate reaches 50 °C/s, the tensile strength, yield strength and hardness can reach 943 MPa, 692 MPa and 300 HV, respectively, which are highly matched with the performance requirements of high-strength pressure vessel steel.

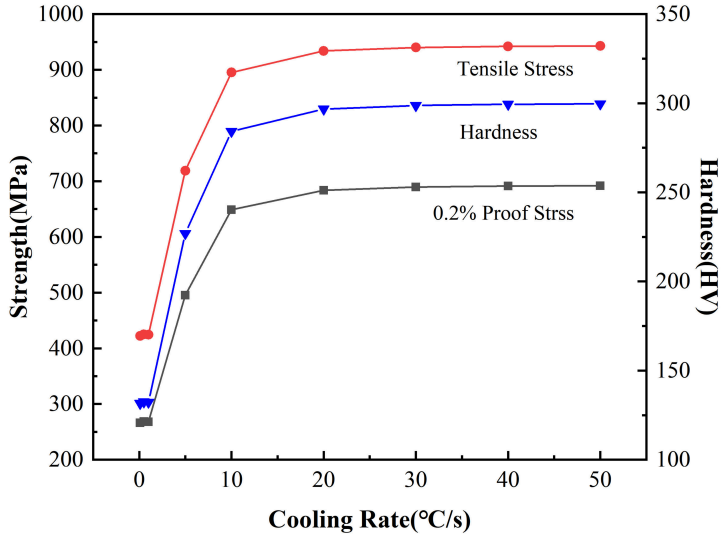


Figure 5. Simulated mechanical performances of Q580R steel.

4. Experimental Results and Analysis

4.1. Microstructure Analysis

Figures 6 and 7 show the room-temperature microstructures of Q580R steel under different cooling rates. The cooling rate exerts a remarkable controlling influence upon phase transformation and microstructure. When the cooling rate is less than 1 °C/s, the microstructure is mainly coarse massive ferrite with a small amount of lamellar pearlite (about 20%). The microstructure is relatively coarse, the mean grain size is roughly 7 μm, and the maximum size can reach 31 μm. When the cooling rate increases to 5 °C/s, a vast number of granular bainite regions appear within the microstructure with a content of about 50%, pearlite disappears, ferrite microstructure is refined remarkably, and the mean grain size decreases to roughly 3 μm. When the cooling rate further rises to 10 °C/s, the ferrite content continuously drops, the bainite content reaches a peak of 59% and becomes the dominant phase. At 20 °C/s, bainite content begins to drop, and a large number of lath martensite regions appear in the microstructure, accounting for about 59%, and ferrite content further decreases to 21%. When the cooling rate increases to 30 °C/s, lath martensite content reaches more than 90%. When the cooling rate reaches 50 °C/s, the microstructure contains almost no bainite; martensite accounts for 99%, existing in the shape of parallel lath bundles, and martensite laths become slender and uniform, with a mean width of about 0.5 μm. Lath martensite serves as the core microstructure for Q580R steel to achieve high strength and excellent toughness matching. Its fine lath structure and high-density dislocations provide a key microstructure support for the synergistic enhancement of steel strength and toughness [34,35]. Comparing the experimental microstructure with the simulation results, it is not difficult to find that the two microstructure evolution laws are in good consistency, both showing the features of decreasing ferrite content, increasing then decreasing bainite, and increasing martensite as the cooling rate rises. There are only small deviations between the experiment and simulation in critical cooling rate and phase content, which are caused by process fluctuations and the interaction of microalloying elements in actual smelting and heat treatment. The overall consistency fully proves the reliability of the JMatPro simulation, and the simulation results can effectively guide the optimization design of the Q580R steel heat treatment process.

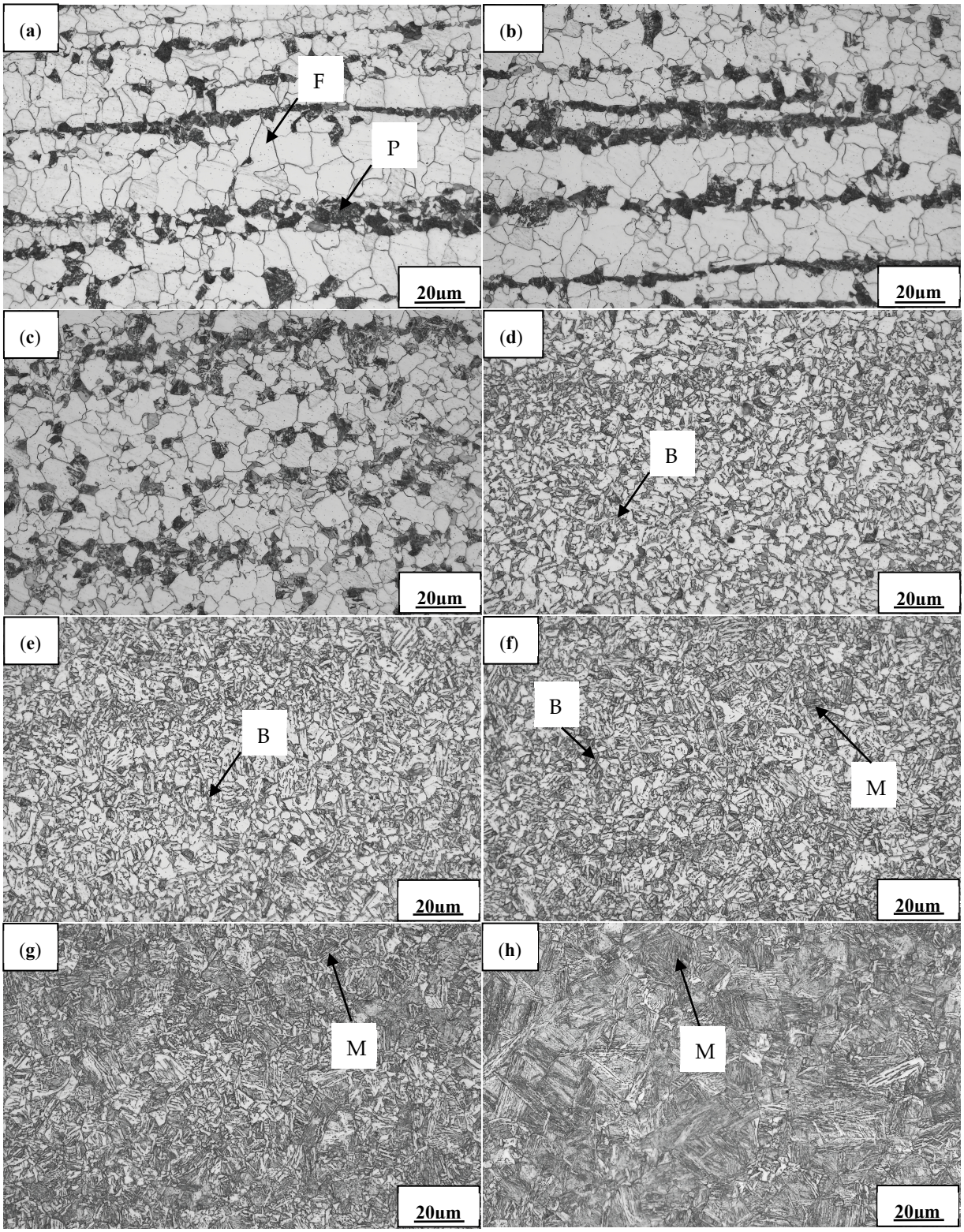


Figure 6. Microstructure of Q580R steel under different cooling rates. (**a**) 0.1 °C/s; (**b**) 0.5 °C/s; (**c**) 1 °C/s; (**d**) 5 °C/s; (**e**) 10 °C/s; (**f**) 20 °C/s; (**g**) 30 °C/s; (**h**) 50 °C/s. F: ferrite; P: Pearlite; B: bainite; M: martensite.

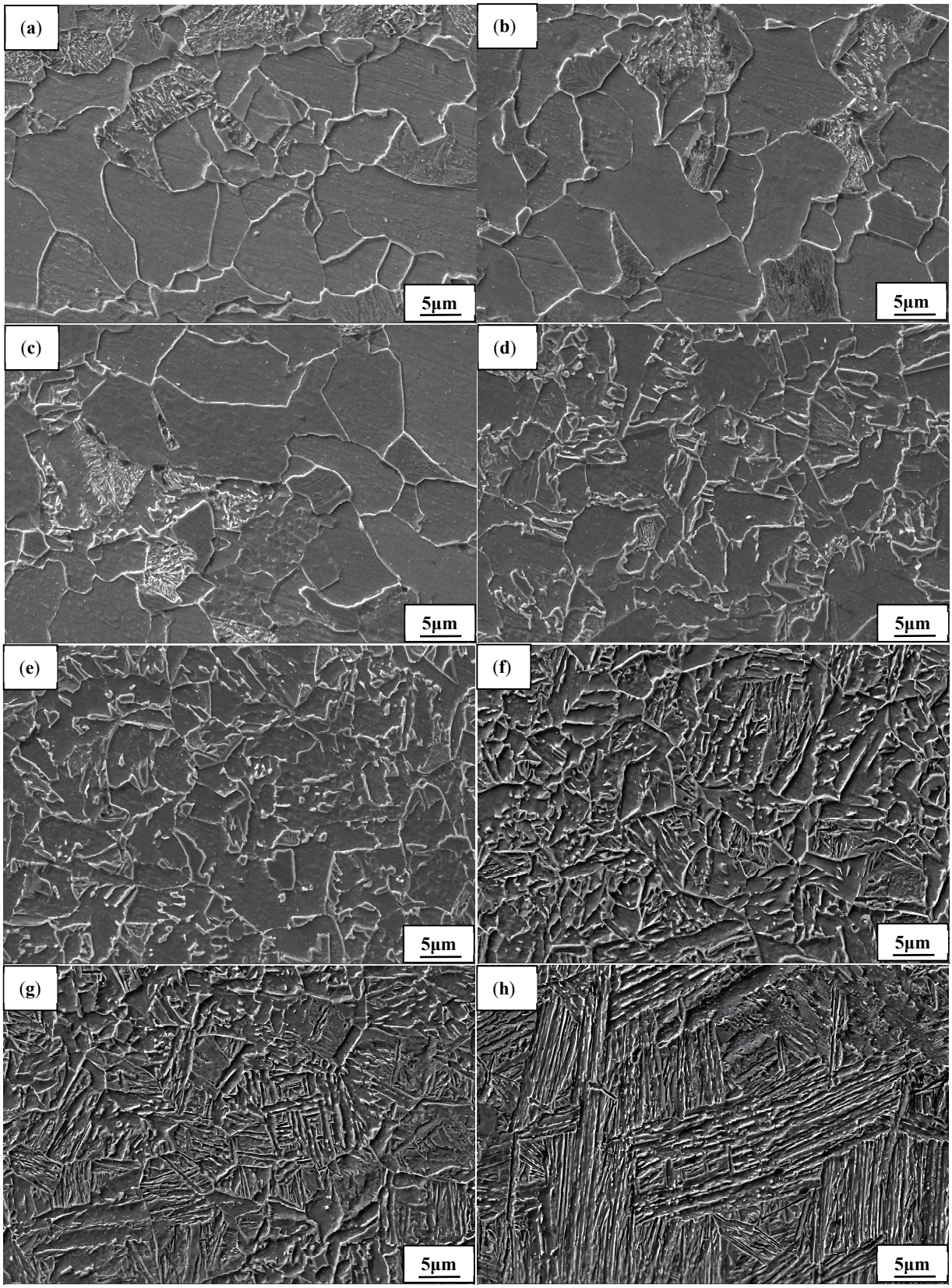


Figure 7. SEM images of Q580R steel under different cooling rates. (**a**) 0.1 °C/s; (**b**) 0.5 °C/s; (**c**) 1 °C/s; (**d**) 5 °C/s; (**e**) 10 °C/s; (**f**) 20 °C/s; (**g**) 30 °C/s; (**h**) 50 °C/s.

4.2. CCT Curve Analysis

According to the Gleeble-3500 thermal simulation dilation curve and microstructure observation results, the measured CCT diagram of Q580R steel was drawn in Figure 8. Evidently, as the cooling rate increases, the phase transformation start temperatures decrease gradually, and the transformation interval moves to a lower temperature as a whole. When the cooling rate is 0.1–1 °C/s, the room-temperature microstructure is ferrite + pearlite. As the cooling rate exceeds 5 °C/s, bainite appears, and ferrite content decreases gradually. As the cooling rate rises to 10 °C/s, bainite content reaches the peak; then, as the cooling rate rises, bainite content progressively decreases and martensite content increases gradually. At 30 °C/s, bainite basically disappears. As the cooling rate is 50 °C/s, the transformation start temperature approaches M_s, and martensite is absolutely dominant in the microstructure. Comparing the measured CCT diagram with the JMatPro simulated CCT diagram, the transformation law, phase composition evolution trend and critical cooling rate interval of the two agree well. Notably, the experimentally measured M_s values fluctuate visibly rather than remaining constant across various cooling rates. This fluctuation originates from alloy elemental microsegregation in practical specimens, inconsistent prior austenite grain sizes among different samples, and unavoidable internal temperature gradients inside Gleeble specimens during cooling. In contrast, JMatPro calculates a fixed single M_s value under ideal uniform composition and homogeneous microstructure conditions. These same factors also account for the 55 °C discrepancy between the average experimental M_s of 496 °C and the simulated M_s of 441 °C. On the whole, the measured results agree well with the simulation results, which fully confirms that the JMatPro software has high reliability in predicting the CCT of Q580R steel. It can provide efficient and reliable theoretical foundations for the rapid screening of the heat treatment, precise design of the cooling system and microstructure control of the steel grade, significantly reducing the number of tests, lessening the research and development cycle as well as costs.

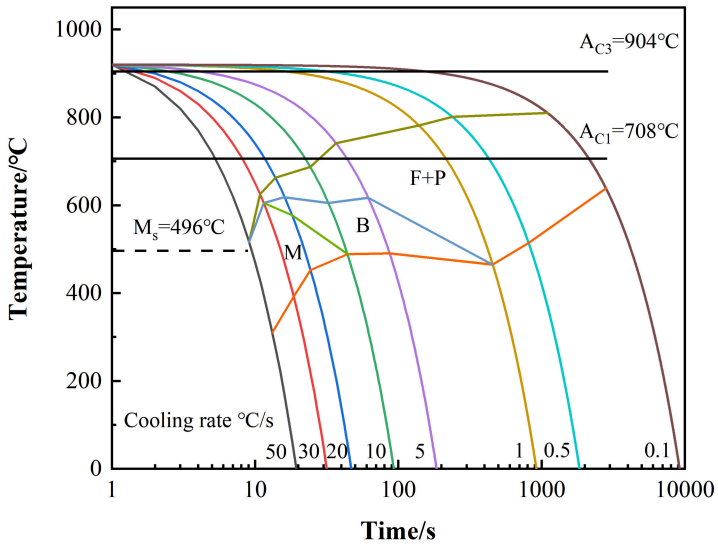


Figure 8. Measured CCT diagrams of the Q580R steel. Colored lines stand for cooling rates (50–0.1 °C/s). A_{C3}, A_{C1}, and M_s serve as the pivotal transformation temperatures. "F + P", "B" and "M" represent ferrite and pearlite, bainite, and martensite regions, respectively.

4.3. Hardness Analysis

Figure 9 compares the experimentally measured hardness with the JMatPro simulated results. The two datasets show nearly identical variation trends: hardness rises rapidly with increasing cooling rate before gradually leveling off. Small numerical discrepancies exist because practical specimens suffer from elemental segregation, non-uniform austenite

grain size, unavoidable temperature fluctuation during testing and residual internal stress, whereas JMatPro calculations are implemented under ideal equilibrium conditions. When the cooling rate is ≤1 °C/s, the microstructure is dominated by soft massive ferrite, so the hardness is low. As the cooling rate rises to 5 °C/s, the hardness increases remarkably. For one thing, the microstructure is prominently refined. For another, a large number of granular bainite regions are formed. The synergy of grain refinement, strengthening and transformation strengthening greatly improves the hardness. As the cooling rate further rises to above 10 °C/s, although the bainite content falls after reaching the peak, lath martensite appears and continues to improve the material's hardness. As the cooling rate exceeds 30 °C/s, martensite works as the predominant phase, the microstructure is dominated by highly refined lath martensite, and the hardness gradually tends to be stable, with a maximum of 308 HV10, which is not much different from the simulated value (300 HV). The consistent evolution between measured and simulated hardness verifies the reliability of JMatPro for correlating cooling rate, microstructure development and mechanical performance of Q580R steel, supplying dependable data for process optimization. Accordingly, the target cooling interval summarized herein can be adopted in industrial production to tailor hardness within the service specification required by pressure vessel design codes.

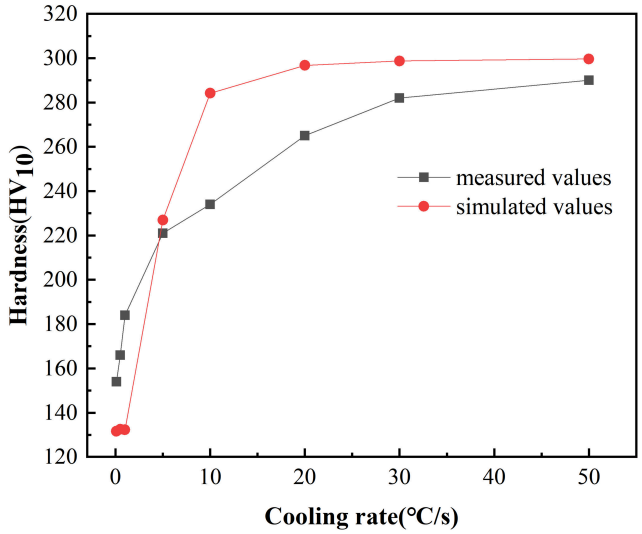


Figure 9. Hardness of Q580R steel at different cooling rates.

5. Conclusions

1. The key transformation parameters of Q580R steel obtained by JMatPro simulation are A_1 = 697 °C, A_3 = 837 °C, M_s = 441 °C, and M_f = 311 °C. With the increase in cooling rate, the ferrite content exhibits a continuous decline, the bainite content rises initially and then declines, while the martensite content increases monotonically; the yield strength, tensile strength and hardness all present a similar variation tendency of "rapid increase first and then stabilization". When the cooling rate ≥ 20 °C/s, martensite accounts for more than 90%, and the hardness is about 300 HV at 50 °C/s.
2. The microstructure of Q580R steel measured experimentally is significantly regulated by cooling rate: as cooling rate ≤1 °C/s, it is chiefly dominated by coarse ferrite + a small amount of pearlite; at 5 °C/s, pearlite disappears and a large number of granular bainite regions appear; at 10 °C/s, bainite content reaches the peak; at 20 °C/s, a large number of lath martensite regions are formed and bainite content decreases; at 30 °C/s, martensite is the dominant phase, occupying more than 90%; at 50 °C/s, martensite accounts for nearly 99%, and the microstructure is uniformly refined. The hardness of Q580R steel rises rapidly first and subsequently tends to be stable as the

cooling rate rises, reaching about 308 HV10 at 50 °C/s. The corresponding strength meets the engineering requirements of low-temperature pressure vessel steel, and the hardness change is highly matched with the microstructure evolution.

3. The experimentally determined CCT diagram, transformation temperatures, microstructure evolution and hardness variation agree well with JMatPro predictions, verifying the software's capability to reliably forecast the phase transformation and mechanical properties of Q580R steel. This approach effectively cuts experimental expenses and shortens process development cycles, delivering practical guidelines for heat treatment formulation of analogous low-temperature high-strength vessel steels. In industrial practice, the critical cooling boundaries identified in this work enable targeted adjustment of online accelerated cooling parameters on production lines, preventing undesirable coarse ferrite or excess martensite and securing long-term safe operation of pressure vessels under fluctuating thermal and mechanical loads.

Author Contributions: W.H.: conceptualization, methodology, investigation, writing—original draft, writing—review and editing; J.W.: experimental supervision and guidance; J.L.: data curation, formal analysis, validation. J.N.: experimental execution; J.B.: software, visualization. All authors have read and agreed to the published version of the manuscript.

Funding: This work was supported by the Foundation of Liaoning Provincial Key Laboratory of Energy Storage and Utilization (Grant No. CNNK202523) and the Youth Research Project of Yingkou Institute of Technology (Grant No. QNL202423).

Data Availability Statement: Data available on request.

Acknowledgments: We appreciate the technical support provided by the experimental platform of Yingkou Institute of Technology during the static thermal simulation experiments and microstructure characterization. Special thanks are given to the colleagues in the research team for their valuable discussions and suggestions throughout the study.

Conflicts of Interest: The authors declare no conflicts of interest.

References

1. Wang, Q.H.; Ye, Q.B.; Wang, Z.D.; Kan, L.Y.; Wang, H.T. Thickness Effect on Microstructure, Strength, and Toughness of a Quenched and Tempered 178 mm Thickness Steel Plate. *Metals* **2020**, *10*, 572. [CrossRef]
2. Chen, S.W.; Xu, H.Y.; Ding, W.J. The Effect of Differential Temperature Rolling on the Deformation of Large Thickness Q345R Steel Plate for Pressure Vessel. *Trans. Indian Inst. Met.* **2025**, *78*, 237. [CrossRef]
3. Bregeault, M.; Clément, D.M.A.; Gloannec, L.B.; Véron, M.R.F.; Landeghem, V.P.H. Evolution of carbon distribution across meso-scale segregations in pressure vessel steel. *Mater. Today Commun.* **2025**, *44*, 112024. [CrossRef]
4. Papin, J.; Delattre, B.J.; Flament, L.J.; Marini, B.; Joly, P.; Mathieu, P.J.; Lorenzon, G.F.A. Effects of quenching and tempering conditions of a low-alloy pressure vessel steel (A508 Gr.3) on its brittle fracture initiation and toughness. *Procedia Struct. Integr.* **2025**, *68*, 727–733. [CrossRef]
5. Sharma, R.; Johnson, A.; Suryavanshi, V.; Dixit, S.; Chaudhari, V. Influence of heat treatments & tempering time on the mechanical properties of SA 387 steel. *Interactions* **2024**, *246*, 17. [CrossRef]
6. Luxenburger, G.; Buchholz, J.; Langenberg, P.; Steffen, M.; Hanus, F.; Cawelius, R.; Wolf, P. High strength quenched and tempered (Q+T) steels for pressure vessels. *Rev. Métallurgie* **2005**, *102*, 919–928. [CrossRef]
7. Zhao, X.Y.; Zou, Y.; Qin, L.Y.; Liu, Y. Effect on properties of HIC resistance vessel steel of quenching and tempering heat treatment. In *Proceedings of 2018 4th International Conference on Applied Materials and Manufacturing Technology*; Shougang Research Institute of Technology, Beijing Key Laboratory of Green Recyclable Process for Iron & Steel Production Technology: Beijing, China, 2018; pp. 500–504.
8. Zhou, L.J.; Dai, J.; Li, Y.; Dai, X.; Xie, C.S.; Li, L.Z.; Chen, L.S. Research Progress of Steels for Nuclear Reactor Pressure Vessels. *Materials* **2022**, *15*, 8761. [CrossRef] [PubMed]
9. Harvanec, J.; Moravec, J.; Mičian, M.; Frátrik, M. Creation of In-Situ Continuous Cooling Transformation Welding Diagrams of S960 High Strength Steel. *Transp. Res. Procedia* **2026**, *93*, 347–352. [CrossRef]

10. Wang, W.S.; Long, X.y.; Zhang, Y.; Li, Y.G.; Sun, X.W.; Yang, Z.N.; Zhang, F.C. Effect of initial phase transformation temperature on the microstructural characteristics and strength-toughness of bainitic steel. *J. Mater. Res. Technol.* **2026**, *40*, 638–650. [CrossRef]
11. Du, Y.; Liu, T.; Zhou, Y.W.; Gao, X.; Wu, H.Y.; Du, L.X. Research on the Continuous Cooling Phase Transformation Behavior of Medium Manganese Steel. In Proceedings of the 9th International Conference on High Strength Low Alloy Steels (HSLA Steels 2025), Nanjing, China, 2–4 November 2025; pp. 91–93.
12. Castro, D.J.P.; Silveira, F.D.C.A.; Rocha, S.D.A.; Stark, A.D.; Sourmail, T.; Epp, J. Impact of hot and warm deformation on the bainite morphology and kinetics during continuous cooling of low- and medium-C carbide-free bainitic steels. *Mater. Des.* **2025**, *257*, 114433. [CrossRef]
13. Zhu, S.T.; Chen, H.Q.; Wang, F.; Hou, H.; Li, N.; Liang, X.X. Effects of Nb-W Microalloying on Continuous Cooling Transformation Behavior and Microstructure Evolution in Low-Alloy Steel. *JOM* **2025**, *77*, 4567–4576. [CrossRef]
14. Yan, Z.M.; Du, Z.Z.; Wang, Q.J.; Yang, T.Y.; Qi, Z.J. Study on Dynamic Continuous Cooling Transformation of 55SiCr Spring Steel. *Metall. Mater. Trans. B* **2025**, *56*, 6046–6058. [CrossRef]
15. Li, J.W.; Li, C.J.; Lu, D.H.; Luo, K.X.; Zhang, S.Z.; Chen, Y.C. Continuous cooling transformation (CCT) diagram of ductile cast iron. *Mater. Lett.* **2025**, *398*, 138977. [CrossRef]
16. Jiang, J.X.; Qin, F.C.; Zhang, L.M.; Zhao, H.L.; Kang, Y.H. The Effect of Composition on the Continuous Cooling Transformation Behavior and Mechanical Properties of HSLA Wear-Resistant Steels. *JOM* **2025**, *77*, 6993–7006. [CrossRef]
17. Zhang, Q.L.; Niu, Q.A.; Chen, Z.J.; Meng, Y.C.; Wang, L.; Dong, H.P.; Yao, J.H. Continuous cooling process of steel 45 in solid phase transformation under laser heat effect. *Opt. Laser Technol.* **2025**, *190*, 113272. [CrossRef]
18. Wang, S.K.; Feng, D.L.; Zhang, Y.Q.; Luo, Y.; Deng, X.T. Effect of Nb microalloying on austenitization, continuous cooling transformation behavior and mechanical properties of seismic-resistant rebar. *Mater. Sci. Eng. A* **2026**, *954*, 149835. [CrossRef]
19. Pei, Y.; Gao, Z.; Liu, Y.; Zhao, S.Q.; Xu, C.Y.; Ren, L.Y.; Li, X.L. Continuous Cooling Transformation Behavior and Phase Transformation Model of Low-Carbon High-Strength Sheet Steel. *Adv. Mater. Res.* **2014**, *1035*, 27–35. [CrossRef]
20. Han, W.N.; Guo, L.L.; Liu, X.Y.; Peng, Y.; Zhang, B. Transformation Behavior of 9Ni Steel Under Continuous Cooling Conditions: Experiments and Simulation. *Crystals* **2026**, *16*, 202. [CrossRef]
21. Pineda, L.F.Z.; Rincón, O.G.; Mata, M.P.G. Austenite Formation and Decomposition in a High-Strength Alloy Subjected to Heating and Cooling Cycles. *Metals* **2026**, *16*, 297. [CrossRef]
22. Dong, D.; Jiang, W.T.; Yan, J.F.; Zhu, D.D.; Fang, N.; Ma, T.F.; Wang, Y.W. Design and investigation on microstructure and properties of Mo-Nb-Ti-V-Si eutectic refractory multi-principal element alloys. *J. Mater. Res. Technol.* **2025**, *37*, 4165–4175. [CrossRef]
23. Krbata, M.; Kohutiar, M.; Escherova, J.; Klučiar, P.; Studeny, Z.; Trembach, B.; Timárová, Ľ. Continuous Cooling Transformation of Tool Steels X153CrMoV12 and 100MnCrW4: Analysis of Microstructure and Hardness Changes. *Appl. Mech.* **2025**, *6*, 16. [CrossRef]
24. Amiri, V.; Moosavy, H.N. Microstructural study of additively-manufactured carbon steel-stainless steel 316L—Inconel 625 functionally graded material: Simulation and experimental approaches. *J. Mater. Res. Technol.* **2024**, *31*, 1164–1170. [CrossRef]
25. Sun, R.C.; Mi, G.B. Influence of Alloying Elements Content on High Temperature Properties of Ti-V-Cr and Ti-Al-V Series Titanium Alloys: A JMatPro Program Calculation Study. *J. Phys. Conf. Ser.* **2023**, *2639*, 012019. [CrossRef]
26. Chen, J.B.; Liu, Y.F.; Wang, Y.J.; Xu, R.; Shi, Q.Y.; Chen, J.S.; Wu, Y.P. Design and Optimization of Heat Treatment Process Parameters for High-Molybdenum-Vanadium High-Speed Steel for Rolls. *Materials* **2023**, *16*, 7103. [CrossRef] [PubMed]
27. Yu, Y.H.; Hou, J.X.; Zhu, P.; Zhang, J.L. Microstructure and properties of iron-based surfacing layer based on JmatPro software simulation calculation. *Vibroeng. Procedia* **2023**, *50*, 180–186. [CrossRef]
28. *GB/T 713.6-2023*; Steel Plates, Sheets and Strip for Pressure Equipments-Part 6: Quenched and Tempered High Strength Steels. Standards Press of China: Beijing, China, 2023.
29. Chinese Mechanical Engineering Society. *Heat Treatment Handbook*, 4th ed.; Volume 2: Structural Steel Heat Treatment; China Machine Press: Beijing, China, 2015.
30. Chen, M.A.; Wu, C.S. The Behavior of Second Phase Particles in a Ti-Nb Microalloyed Steel During Welding Thermal Cycle. *Adv. Mater. Res.* **2014**, *936*, 1786–1790. [CrossRef]
31. Jin, Y.L.; Du, S.L. Precipitation behaviour and control of TiN inclusions in rail steels. *Ironmak. Steelmak.* **2018**, *45*, 224–229.
32. Li, Q.D.; Chen, Y.H.; Liu, C.W.; Gu, J.F. Compositional Variants of Cu-rich Precipitate in Thermal-Aged Ferritic Steel. *Acta Metall. Sin. (Engl. Lett.)* **2017**, *31*, 364–370. [CrossRef]
33. Niino, T.; Inoue, J.; Ojima, M.; Nambu, S.; Koseki, T. Effects of Solute Carbon on the Work Hardening Behavior of Lath Martensite in Low-Carbon Steel. *ISIJ Int.* **2017**, *57*, 181–188. [CrossRef]

34. Zhao, Y.; Tong, X.; Wei, X.H.; Xu, S.S.; Lan, S.; Wang, X.L.; Zhang, Z.W. Effects of microstructure on crack resistance and low-temperature toughness of ultra-low carbon high strength steel. *Int. J. Plast.* **2019**, *116*, 203–215. [CrossRef]
35. Mirzaei, A.; Barrett, C.D.; Ma, X.; Hodgson, P.D.; Beladi, H. New Insight into Toughness Enhancement in a Lath Martensitic Steel. *Metall. Mater. Trans. A* **2024**, *55*, 1409–1417. [CrossRef]

Disclaimer/Publisher's Note: The statements, opinions and data contained in all publications are solely those of the individual author(s) and contributor(s) and not of MDPI and/or the editor(s). MDPI and/or the editor(s) disclaim responsibility for any injury to people or property resulting from any ideas, methods, instructions or products referred to in the content.